InSAR-Derived Coastal Subsidence Reveals New Inundation Scenarios Over the Yellow River Delta

Peng Li [ID], Guoyang Wang [ID], Cunren Liang [ID], Houjie Wang [ID], and Zhenhong Li [ID], *Senior Member, IEEE*

Abstract—Coastal subsidence exacerbates relative sea level rise (SLR) and increases the risk of coastal flooding. However, the contribution of local land subsidence (LLS) in the Yellow river delta (YRD) to the relative SLR remains unclear, leading to a gap in the understanding of future inundation scenarios. In this article, we firstly used five years of Sentinel-1 data to generate the high-accuracy coastal subsidence of the YRD. Radar interferometry (InSAR) results show that fast subsiding funnels larger than 50 mm/yr are mainly distributed in the brine mining clusters, and the maximum subsidence rate exceeds 300 mm/yr. We then proposed an inundation estimation method by combining extended seeded region growing model, InSAR-derived LLS and SLR. This method can effectively output the coastal inundation time series, quantify and characterize the changes of inundation area and depth without detailed hydrodynamic conditions. Moreover, we presented high spatiotemporal resolution inundation scenarios for the entire YRD, revealing that in the absence of control measures, annual subsidence of 19 mm/yr contributes at least three times more than that SLR to the increased flood risk in 2050 under the low greenhouse gas emissions scenario (SSP1-2.6). However, under the scenario of SSP5-8.5, 4611 km^2 of land would be inundated by 2100 and coastal dams are extremely likely to be damaged. This article is expected to provide a practical and cost-effective alternative to understanding the contribution of coastal subsidence to the relative SLR, and for choosing when and how to mitigate land subsidence to prevent future coastal flooding in the delta.

Index Terms—Coastal flooding, coastal subsidence, interferometry (InSAR), inundation scenario, sea level rise (SLR), Yellow river delta (YRD).

Peng Li, Guoyang Wang, and Houjie Wang are with the Institute of Estuarine and Coastal Zone, College of Marine Geosciences, Key Laboratory of Submarine Geosciences and Prospecting Technology, Ministry of Education, Ocean University of China, Qingdao 266100, China, and also with the Laboratory of Marine Geology, Qingdao National Laboratory for Marine Science and Technology, Qingdao 266061, China (e-mail: pengli@ouc.edu.cn; wgy0318@stu.ouc.edu.cn; hjwang@ouc.edu.cn).

Cunren Liang is with the Institute of Remote Sensing and Geographic Information System, School of Earth and Space Sciences, Peking University, Beijing 100871, China (e-mail: cunren.liang@pku.edu.cn).

Zhenhong Li is with the College of Geological Engineering and Geomatics, Chang'an University, Xi'an 710054, China, also with the Big Data Center for Geosciences and Satellites (BDCGS), Xi'an 710054, China, also with the Key Laboratory of Western China's Mineral Resource and Geological Engineering, Ministry of Education, Xi'an 710054, China, and also with the Key Laboratory of Ecological Geology and Disaster Prevention, Ministry of Natural Resources, Xi'an 710054, China (e-mail: zhenhong.li@chd.edu.cn).

Digital Object Identifier 10.1109/JSTARS.2023.3272782

I. INTRODUCTION

COASTAL deltas are generally low-lying and highly vulnerable to sea level rise (SLR), while local land subsidence (LLS) exacerbates coastal flooding risk [1], [2], [3]. Although coastal infrastructure and human settlements are located at elevations slightly above normal sea level, the relative SLR are leading to the salinization of farmland, damage to infrastructure, and loss of human habitation through coastal erosion, seawater intrusion [4], [5], [6]. Among them, coastal flooding and inundation is the primary coastal response to the relative SLR [4], [7], [8], [9]. Therefore, there is a pressing need to understand what and to what extent contributes to the risk of coastal flooding through better observation and modeling, which is crucial for coastal environmental protection and sustainable development [5], [10], [11], [12], [13], [14], [15], [16], [17].

Coastal subsidence mainly comes from the exploitation of oil and natural gas in the underlying sediment, and the extraction of water for industry, agriculture and daily life [18], which leads to the reduction of ground elevation, the destruction of coastal protection engineering, the decline of levees against seawater intrusion, the increase of inundation depth and the shortening of flood return period [17], [19], [20], [21]. Consequently, the LLS is becoming a non-negligible driver to coastal flooding [2], [20]. However, the quantitative characterization of the contribution of coastal subsidence to the relative SLR is still lacking [18], [22], especially for the Yellow river delta (YRD), the widest, most complete, and youngest delta both in China and the world [23].

On the one hand, the information on the extent of coastal subsidence and its effects on global river deltas is scarce, with mitigation measures being implemented in only a few locations [22]. Measurements from traditional leveling and global navigation satellite system have high accuracy, but far from enough spatial resolution, high labor intensity and low efficiency. At present, time series analysis of synthetic aperture radar interferometry (TS-InSAR) have provided an all-weather, day-and-night monitoring capacity at an unprecedented spatial coverage and resolution [18], which has great advantages compared with traditional methods [24], [25], [26], [27], and has been widely used in land subsidence monitoring [5], [15], [16], [18], [20], [28].

On the other hand, modeling coastal flooding for future disaster projections is a challenging task, due to the contribution of various intertwined processes. Hydraulic model [29], [30], [31] and hydrostatic model [32], [33], [34] are two commonly used models for inundation assessment. The former is capable of continuous fine simulation on a short time scale, but with many and complex parameters, it is difficult to consider terrain

changes [35], while the latter (also known as simplified model) is easy to be superimposed with digital elevation model (DEM), and water level [20], [33]. For simple plain terrain, the difference between the two models is not significant in the extent and depth of inundation [36]. However, the number of parameters and computation burden of the simplified model are obviously lower than that of hydrodynamic model. Bathtub model is a widely used simplified model to simulate future inundation scenario [19], [20], [33], [37], but tends to overestimate the inundation area [5], [17], [20]. In addition, few existing models can output the time series of flooded areas, making it difficult to find the possible time nodes and spatial locations of sudden increase of flood range.

In this article, we will carry out the simulation of future inundation scenario, aiming at providing useful reference for coastal inundation mitigation, adaptation and retreat. First, we use five years of Sentinel-1 data to generate the high-accuracy coastal LLS over the entire YRD. Then, we propose a method combining extended seeded region growing (ESRG) model with the LLS and SLR to project annual flood evolution at a spatial resolution of 30 m. Furthermore, we present the inundation scenarios in the YRD at high spatiotemporal resolution and discuss the uncertainties of the results.

II. STUDY AREA

As shown in Fig. 1(a), the study area is located in the northern coast of Shandong Province, China [23], [38], [39], [40], [41], covering an area of about 9400 km^2. The YRD in the conventional sense is completely included. According to Fig. 1(b), the area below 2 m above sea level is about 4270 km^2, accounting for 45.4% of the total area. Sediment is the physical medium of coastal subsidence, and its thickness distribution is shown in Fig. 1(c), decreasing from coastal to inland. According to Syvitski, et al. [2], this area is extremely vulnerable to flooding risk due to the continued SLR. In addition, the YRD is dominated by oil fields, aquaculture farms, and salt pans, resulting in severe land subsidence. At present, researchers have analyzed the correlation between environmental change and flood risk in some areas of China, such as the Yangtze river delta [16]. However, there are still few flood modeling and inundation scenario analysis considering the contribution of large-scale detailed coastal subsidence in the YRD [13], [19], [42], [43], [44].

Along most of the coastline of the YRD, earth-rock dams have been built to protect the land from sea intrusion. Most of the time, these coastal dams can effectively withstand daily wind waves and storm surges. However, when storm surge, astronomical spring tide and rainstorm occur simultaneously, there would be a great possibility of overtop and dam failure.

III. DATASETS AND METHODOLOGY

The ESRG method proposed in this article can output inundation time series with a customized time interval in a long-time span. The time series mentioned here is different from the inundation process of a single flood output by the hydraulic model, but refers to the year-by-year evolution of the inundation range under the combined effect of SLR and LLS. TS-InSAR
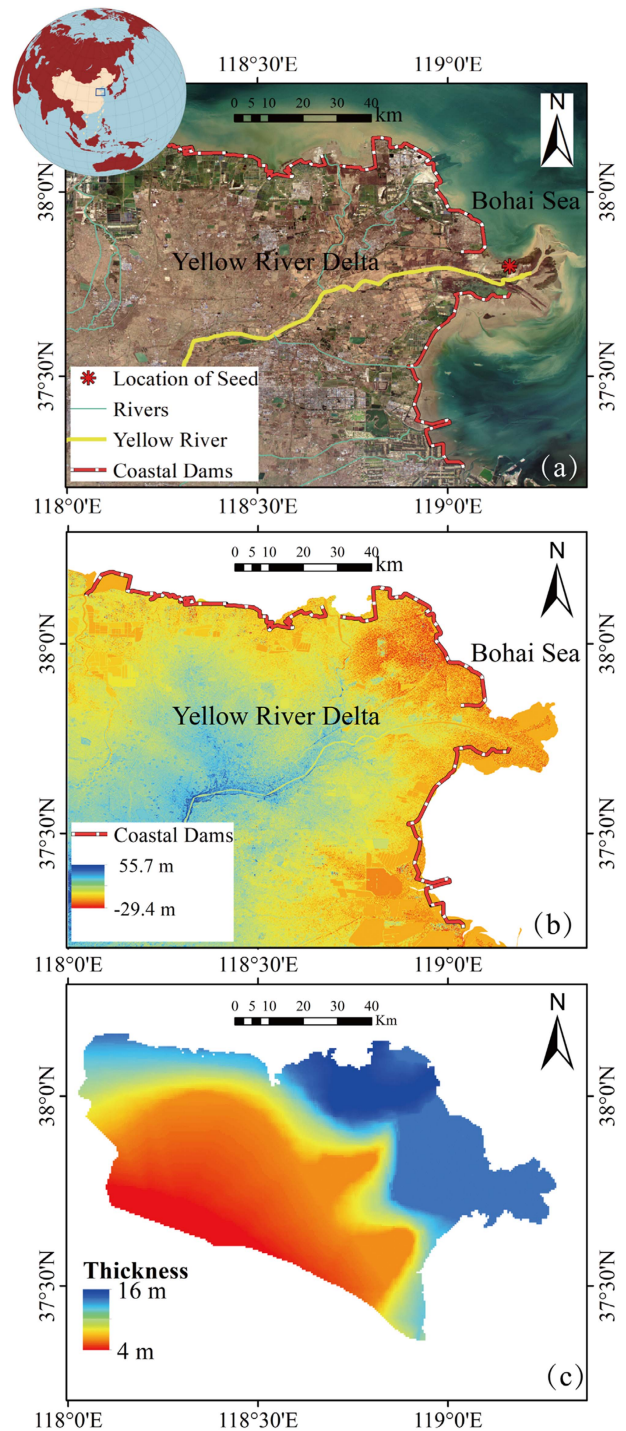

Fig. 1. (a) Study area. (b) Distribution of coastal dams. (c) Deposit layer thickness in the YRD. Note that, this article area is larger than the modern YRD.

are adopted to ensure the accessibility and reliability of large scale and high resolution LLS.

The workflow consists of the following three steps.

1) *Data Preparation:* The primary datasets are given in Table I. The SLR projections in different shared socioeconomic pathways (SSPs) released from the sixth assessment report of the intergovernmental panel on climate change (IPCC) are employed [45]. The SSPs are scenarios of projected socioeconomic global changes used to derive

Datasets	Description
DEM	30m NASADEM
Sentinel-1 SAR images	Ascending track no. 69, 2017/03−2020/11 (109 scenes); Descending track no. 76, 2016/10−2020/11 (106 scenes)
SLR from IPCC AR6 Storm surge	SSP1-2.6, SSP2-4.5 and SSP5-8.5 72−155cm
Average sea level from tide gauge	-56.8 cm in EGM96 height datum

greenhouse gas emissions scenarios with different climate policies.

2) *Data Preprocessing:* This step includes coastal vertical land motion (VLM) estimation by TS-InSAR, deformation trend assumption, and sea level simulation.

3) *Inundation Assessment:* Inundation-prone area estimation based on the ESRG model, InSAR-derived LLS and SLR.

A. InSAR-Derived Coastal Subsidence

TS-InSAR is an effective method to provide coastal subsidence product with large spatial coverage (100–500 km) and high spatial resolution (1–20 m) to characterize the LLS. Persistent Scatterers InSAR [26] and small baseline analysis InSAR [24] are the two common TS-InSAR algorithms. The latter is more suitable for nonurban areas, such as the YRD. In addition, the InSAR-derived coastal subsidence can be conveniently combined with current DEM to simulate future topography.

In this article, we used GAMMA and LiCSBAS softwares for the interferometric processing and SBAS processing [46], [47] with four years of Copernicus Sentinel-1 SAR images from the European Space Agency (ESA) to estimate the coastal subsidence across the whole YRD (see Table I). Before interferogram generation, the height datum of DEM is converted from EGM96 geoid to WGS84 ellipsoid according to (1) to avoid the errors caused by the inconsistent height datum between DEM and SAR images [48]

$$DEM_{WGS} = DEM_{EGM} + \Delta h. \tag{1}$$

Here, DEM_{WGS} is the DEM with WGS84 height datum, DEM_{EGM} is the DEM with EGM96 height datum, and $\triangle h$ is the geoid height.

The SBAS time series analysis method itself can filter the atmospheric error of the unwrapping interferograms by means of spatiotemporal filtering and smoothing, but the premise is that the tropospheric delay is random in time and the surface deformation is stable throughout the smoothing or average period [24]. However, the unwrapping interferogram contains many significant errors that cannot be eliminated simply by statistical smoothing or spatiotemporal filtering, such as tropospheric and ionospheric delay errors, topography errors, and unwrapping errors [49], [50], [51], [52], [53]. If no preprocessing is conducted, the results will still have great uncertainty. Previous studies have shown that external estimation and correction of atmospheric delay errors in interferogram prior to time series analysis can significantly reduce atmospheric errors and help improve the accuracy of deformation monitoring [54], [55].

We firstly used GACOS products to remove the tropospheric delay by subtracting the GACOS phases from the unwrapped interferograms to obtain the corrected interferograms [54]. Split-spectrum method can effectively estimate and correct the ionospheric phase error caused by the spatiotemporal variation of electron density [56]. Considering that the ionospheric phase is mostly long-wavelength signal, and there is no obvious long-wavelength deformation pattern in this article, we then used the quadratic fitting method to correct the ionospheric errors of the interferograms [55]. The final deformation rate results were filtered by the LiCSBAS software. Specifically, the Gaussian kernel is used for high-pass in time and low-pass in space to further reduce the noises and improve the signal-to-noise ratio of the real deformation signals.

According to the following (2), and assuming that the horizontal deformation can be ignored due to the absence of large active faults and extensive seismic activities [57], [58], [59], VLM rate can be decomposed by the deformation rate in line of sight (LOS)

$$V_{VLM} = V_{LOS}/\cos\theta \tag{2}$$

where V_{VLM} is the VLM rate, V_{LOS} is the rate in LOS direction, and θ is the incidence angle of each pixel.

As shown in Fig. 2(a) and (b), the average subsidence rate of the whole YRD is 19 mm/yr, which is already much higher than the current SLR rate. Fast subsiding funnels larger than 50 mm/yr are mainly distributed in the coastal brine mining clusters, and the maximum subsidence rate exceeds 300 mm/yr. The VLM map will be used for the following DEM simulation. Leveling data and cross-validation of different orbits are used to evaluate the accuracy of the InSAR deformation rate map. Traditional and robust accuracy measures are used for the assessment of the accuracy due to potential outliers or non-normality of error distribution, including the standard deviation (STD), Spearman's correlation (Corr), root-mean-square error (RMS), mean, median, median absolute deviation (MAD), normal MAD, and 90% linear error (LE90) [19], [60], [61]. As shown in Fig. 2(c), 7 792 279 points between two VLM maps are extracted to validate the accuracy. The correlation between the two tracks is as high as 0.84. A mean difference of about −1.4 mm/yr and an RMS value of 12.7 mm/yr are obtained, while the median and LE90 are −0.6 mm/yr and 11.5 mm/yr, respectively. It can be seen from Fig. 2(d) that the correlation between InSAR-derived subsidence and field leveling is as high as 0.96. The mean, STD, RMS, median, MAD, and LE90 values are all lower than 7.5 mm/yr.

B. DEM Simulation

We used the newly released one-arc-second (30 m) NASA-DEM (https://www.earthdata.nasa.gov/) derived from a combination of shuttle radar topography mission (SRTM) processing improvements, elevation control, void-filling and merging with data unavailable at the time of the original SRTM production.
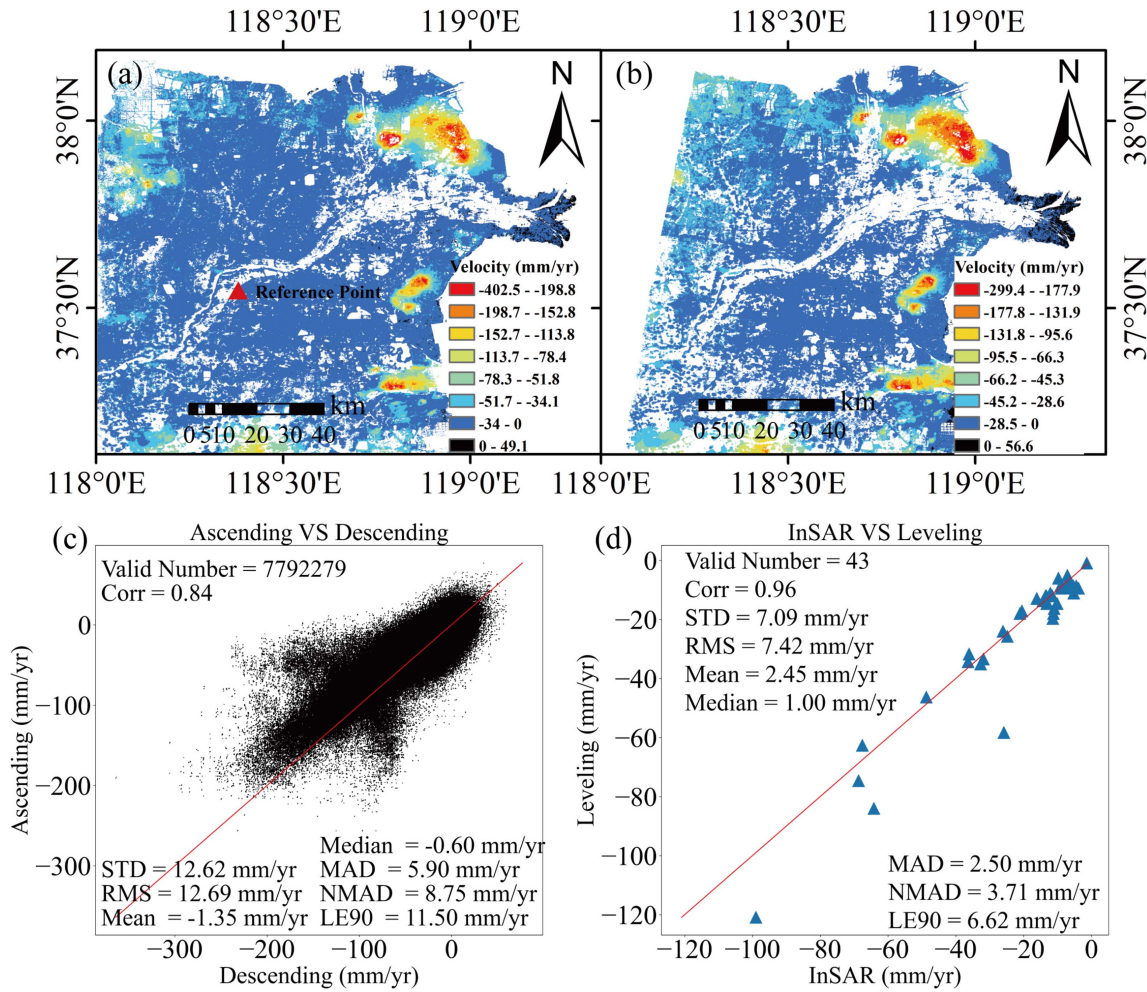
Fig. 2. VLM maps and accuracy evaluation. (a) and (b) Ascending and descending VLM maps in 2019–2020, respectively. (c) Comparison between ascending and descending deformation rate maps. (d) Comparison between ascending deformation rate and leveling data. Note that, this study area is larger than the modern YRD. The red triangle represents the reference point (118.376349°E, 37.547983°N).

We used ice, cloud, and land elevation satellite (ICESat) altimetric data to evaluate the elevation accuracy of NASA-DEM. The ICESat was a NASA satellite mission for measuring ice sheet mass balance, cloud and aerosol heights, as well as land topography and vegetation characteristics. The sole instrument on ICESat was the geoscience laser altimeter system (GLAS), a space-based light detection and ranging (LiDAR). GLAS combined a precision surface LiDAR with a sensitive dual-wavelength cloud and aerosol LiDar. Over most of the ice sheets, the accuracy of each surface elevation measurement is 15 cm, averaged over 60 m diameter laser footprints spaced at 172 m along-track [62]. As shown in Fig. 3(a), the yellow lines are the high-quality ground control points used for the accuracy assessment, which are generated from ICESat GLAS measurements. The correlation of 0.83 between NASADEM and ICESat is shown in Fig. 3(b). A mean difference of about −0.3 m and an RMS value of 1.1 m are obtained, while the median and LE90 are −0.3 and 1.1 m, respectively. In fact, the terrain of the YRD is so flat that it is completely different from the mountains, with few noticeable fluctuations, so the elevation accuracy of NASADEM is credible.

Previous studies have shown that the coastal subsidence of the YRD was not as serious before 2010 as it is today [59], [63], [64]. Meanwhile, due to the limitation of InSAR observations available at that time, the monitoring accuracy and spatiotemporal resolution are relatively poor. At present, continuous observation of Sentinel-1 provides necessary conditions for better monitoring of coastal subsidence [57], [65]. Principal component analysis (PCA) can derive the variance contributions and eigenvectors of the InSAR time series to characterize the dominant temporal behavior of the deformation [28], [66], [67], [68], [69]. As shown in Fig. 4, we find that the variance contribution rate of the first principal component (PC1) to the whole subsidence in the study area is 95.75%. The eigenvector of PC1 increases linearly and steadily, indicating that the driving factors corresponding to PC1 had a positive effect on land subsidence. Therefore, we can confirm that the dominant subsidence trend from 2016 to 2020 is almost linear.

Our previous study has shown that in the areas with the most severe coastal subsidence in the YRD, human activities related to underground brine mining contribute more than 94% to subsidence, while other driving factors, such as precipitation,
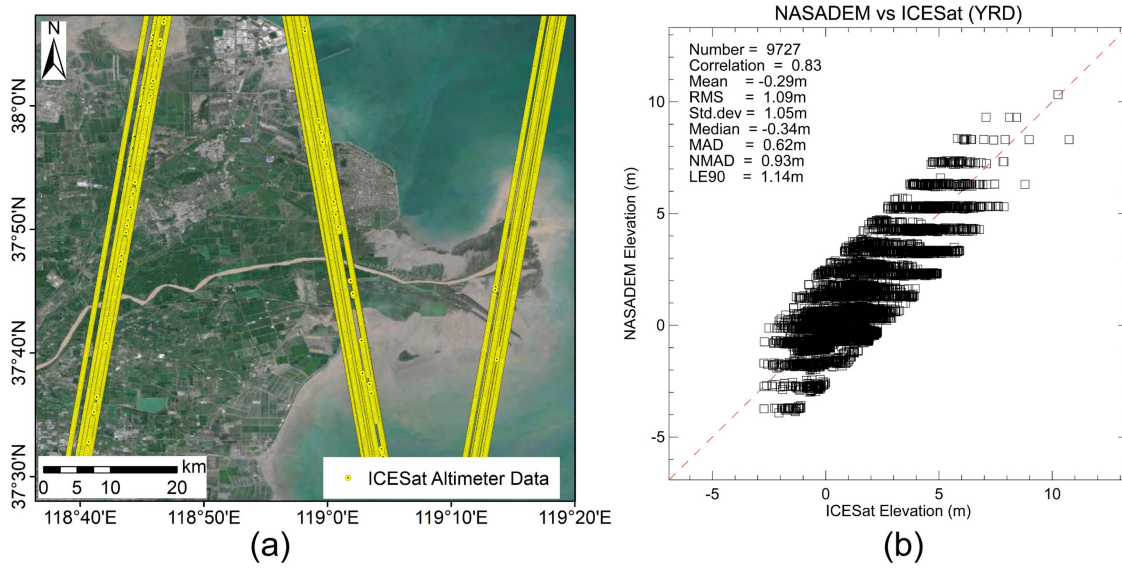
Fig. 3. (a) Distribution of ICESat altimeter data. (b) Accuracy evaluation of NASADEM by comparison with ICESat.
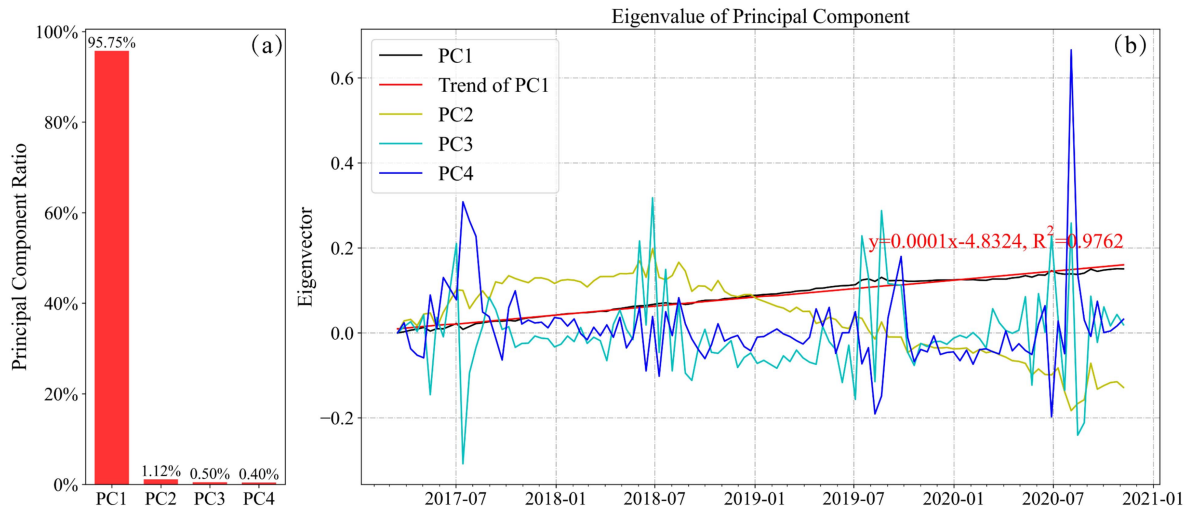

Fig. 4. Variance contributions and temporal change of eigenvectors from PCA. (a) Rate of PCs' variance contribution. (b) Temporal rule of eigenvectors, the red solid line is the best fitting regression of PC1.

soil consolidation, oil extraction, and other activities are not noticeable [28]. Given the demand for halogens and oil and gas due to socio-economic development, there is no indication that the extraction of underground fluids, such as brine and oil will be reduced or stopped in the next 10–20 years. Therefore, we assume that the trends of land subsidence remain unchanged in the future and will continue until 2100. Note that this assumption is relatively reliable in the short term, but the model of the long-term projection may need to be adjusted as more observations are available. As shown in (3), we use a simple linear model to simulate the change of topography, which has been widely used in previous studies [5], [20], [70]

$$\mathrm{DEM_t} = \bar{v}t + \mathrm{DEM_0} \qquad (3)$$

DEM_t is the future elevation and t is the time interval between 2020 and corresponding scenario, $\bar{v}$ is the rate of InSAR-derived LLS, DEM_0 is the original elevation.

C. Water Level Simulation

Severe coastal floods are often caused by the superposition of storm surge and astronomical spring tide. Therefore, sea levels used in inundation assessment are usually simulated by the superposition of the astronomical tides, storm surges and SLR [19]. However, inundation is a process that requires sustained, rather than instantaneous high-water levels. Therefore, mean water levels were obtained from 2018–2019 tide observations, rather than astronomical spring tide levels, to prevent overestimating inundation. The average water level is 0.11 m, whilst the highest storm surge recorded in recent years was 1.55 m.

Note that the sea level height datum is consistent with the DEM, and the deviation of elevation system is 0.68 m. The simulated sea level (SSL) is expressed in (4), and the result is shown in Fig. 5

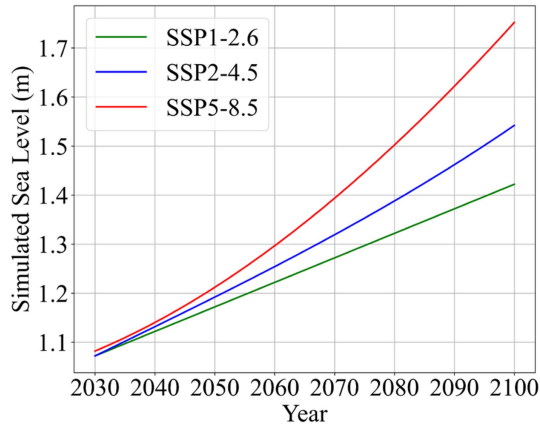$$\mathrm{SSL}_t = \mathrm{MSL} + \mathrm{MSS} + \mathrm{SLR}(t). \qquad (4)$$

Fig. 5.   Sea level simulation under different SSPs from 2030 to 2100.
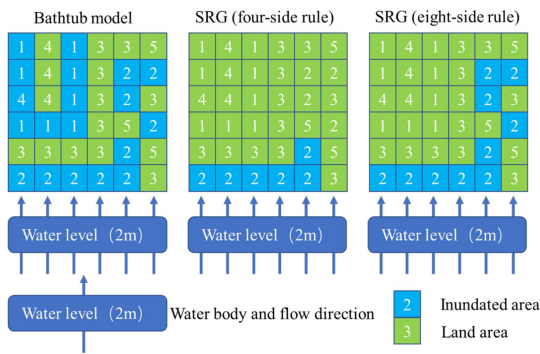

Fig. 6.   Sea level simulation under different SSPs from 2030 to 2100.

MSL is the mean sea level from long-term tidal data and MSS is the maximum value of storm surge in the last 20 years. SLR(t) is the projected SLR under different SSP scenarios.

D. Inundation Models

Unlike the bathtub model without hydrological connectivity, the seeded region growing (SRG) model with eight-side connectivity rule [34], [71], [72], [73] takes into account the obstruction of water flow by topographic relief and ensures that all inundated areas are spatially connected as shown in Fig. 6. It can effectively avoid the inappropriate analysis of the cratered mountain topography and dam enclosure area. Therefore, the SRG model is more suitable than the traditional bathtub model in cases with many gullies, buildings, or land cover.

There are only two variables in traditional SRG model, the fixed water level and elevation. In this article, we construct the ESRG model, which takes the location of the "seed" point, time-varying (t) coastal subsidence (vt), initial topography (DEM$_0$), and simulated sea level (SSL) change as input, and exports inundation time series with a grid size of 30 m. As shown in Fig. 7, both time resolution (r) and time span (n) can be customized to control the termination of the ESRG loop. In this article, we set the time span from 2030 to 2100 with a step of one year.

As for the selection of seed points, Fig. 1 shows that only the tidal flat area at the estuary of the YRD has the lowest elevation
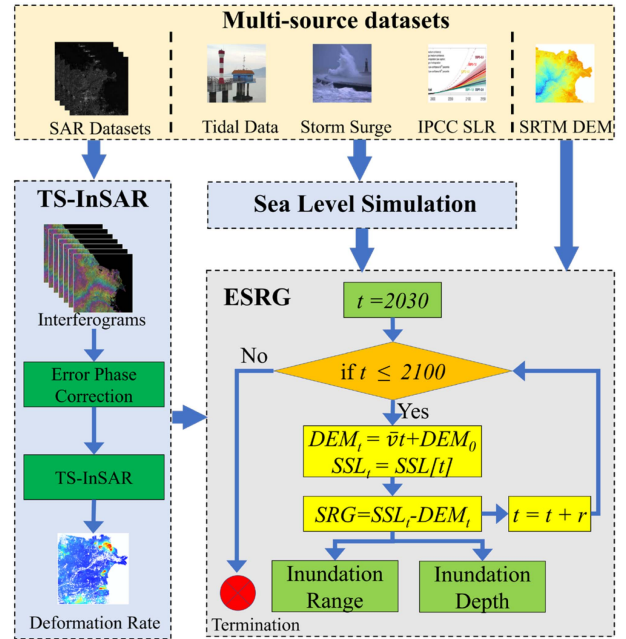

Fig. 7.   Flowchart of the coastal inundation estimation method proposed in this article.
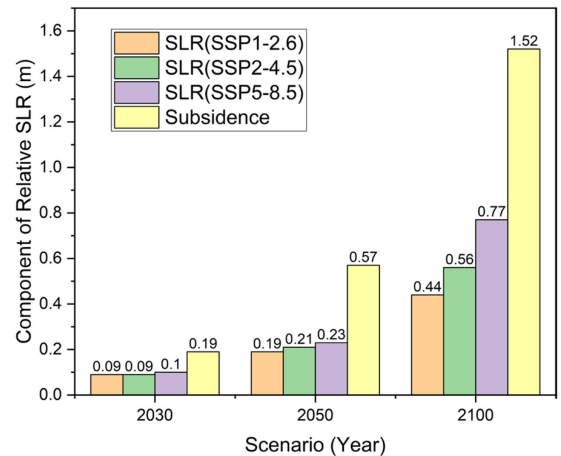

Fig. 8.   Bar graph with SLR and subsidence of the YRD under three scenarios in 2030, 2050, and 2100. Note that the rates of SLR under were derived from IPCC AR6. We assume that the land subsidence increases linearly and the mean subsidence rate of 19 mm/yr remains constant.

and is not protected by a bank dam with a high design standard, making it more likely to be flooded first. Therefore, we chose the "seed" of the estuarine region as the starting point of the ESRG model.

IV. RESULTS AND DISCUSSION

A. Future Inundation Scenarios

As shown in Fig. 8, under the scenario of SSP1-2.6, the sea level will slowly rise from 9 to 44 cm in the next 10–80 years. Considering that the average subsidence rate of the whole YRD is 19 mm/yr, which is already much higher than the current IPCC published SLR rate, if no control measures are taken, the average

TABLE II
DEFINITION OF THE INUNDATION MODELS

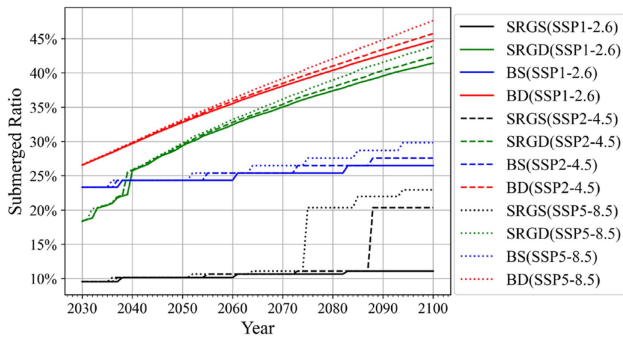| Models	Definition
BS	The Bathtub model with Singe variable (water level only)
BD	The Bathtub model with Double variables (LLS and water level)
SRGS	The SRG model with Singe variable (water level only)
SRGD	The SRG model with Double variables (LLS and water level)

Fig. 9. Inundated pixels of the YRD from 2030 to 2100. Different line types represent different models for a given SSP. Different colors represent different SSPs for a given model.

coastal subsidence will deteriorate from 19 cm in 2030 to 152 cm in 2100. Consequently, the contribution of coastal subsidence to the relative SLR in 2050 will be at least three times greater than SLR under the low emission scenario.

As given in Table II and Fig. 9, inundation scenarios were estimated using univariate (BS) and bivariate (BD) bathtub models and univariate (SRGS) and bivariate (SRGD) SRG models, respectively. SRGS and BS models only consider SLR, while both SRGD and BD models take SLR and LLS as input parameters. The BS, BD and SRGS were used as control groups to illustrate the rationality and validity of SRGD.

Bathtub models for the red and blue lines present a higher estimation than those of the ESRG models, regardless of whether the LLS is considered. However, the intensification of LLS is causing a considerable rise in relative sea level, and undulating terrain is increasingly difficult to prevent the spread of coastal flooding. Therefore, the range of inundation estimated by the BD and SRGD models gradually narrowed over time.

Interestingly, the SRGS results in black lines show obvious mutations. The reason is that the sea level continues to rise and eventually breaks through the constraints of the topography or dam, resulting in overtopping. Under the scenario of SSP5-8.5, the flood resistance of the YRD may not decrease significantly until 2070. Therefore, we believe that the ability of coastal flood resistance of the YRD will not decrease significantly in a short time when only SLR is considered.

The inundated pixels estimated by the SRGD increase significantly with time. Before 2070, the results are even three times higher than those of the SRGS model under the scenario of

SSP5-8.5. Therefore, it can be inferred that with the increased subsidence, topographic constraint on flooding is significantly weakened, leading to a significant increase in the risk of flood exposure in the open sea.

If the elevation of a raster cell is lower than the predicted sea level, the BS and BD models that does not account for hydrological connectivity would consider the raster cell to be flooded. Therefore, as shown in the left two columns of Fig. 10(a), (b) and (c), there are many inundation outliers in the raster cells estimated by the bathtub model, which is inconsistent with the spreading of the coastal flooding. In addition, the bathtub model estimates did not change much over time in terms of the inundated area. Although the topography of the study area was simple and flat, there was a large deviation between the flooded area estimated by the bathtub model and that estimated by the SRG model. Therefore, to avoid the above false overestimation, the SRG model is more suitable for coastal flood risk assessment.

The SRGS results only consider SLR due to climate change, while the SRGD results take into account both LLS and SLR. Under the SSP5-8.5 scenario, the SRGD model that considers the continuous LLS and SLR from 2030 to 2100, projects the vulnerable inundated area from 2233 to 4611 km^2, as opposed to 1188–2758 km^2 with SLR only. By 2100, under the scenario of SSP1-2.6, SSP2-4.5 and SSP5-8.5, SRGD estimated 30%, 22% and 21% more flooded pixels than SRGS, respectively. Moreover, compared with the SLR, coastal subsidence brings a greater risk of flooding in the YRD not only in inundation area but also in inundation depth. The great inundation depth of 30 m in some areas is mainly attributed to the fact that the local subsidence rate in this area is indeed relatively large (>300 mm/yr), which is 15 times higher than the average rate (19 mm/yr). Although the proportion of such extremes is generally low, recent studies have also shown that the flood threat caused by coastal subsidence is significantly greater than the SLR caused by climate change by a factor of 3–5 or more [5], [8], [12], [18], [22].

As shown in the third columns of Fig. 10(a)–(c), some low-lying areas are highly vulnerable to coastal flooding. These easily flooded areas cover a wide range and coincide with the areas with severe subsidence shown in Fig. 2, which greatly increases the difficulty of human engineering to protect the land. However, these areas can be artificially isolated by dams perpendicular to the shoreline. Therefore, dams can be placed on the upper and lower sides of the area to effectively reduce the random spread of floods, as shown by the solid red line in Fig. 11.

The inundation estimation derived by combining the ESRG model, SLR and LLS can conveniently and intuitively show the annual inundation evolution, quickly identify the area susceptible to inundation, and output inundation time series with less calculation and faster computation speed. By extracting the information contained in the inundation time series, it can help to identify high-risk areas and guide the construction of engineering projects. As the LLS is changing and the SLR projection is constantly adjusted by the IPCC, the input parameters of the proposed method need to be adjusted in time with the release of new data. In addition, satellite earth observations continue to provide available data sets that can be used to update the input data.
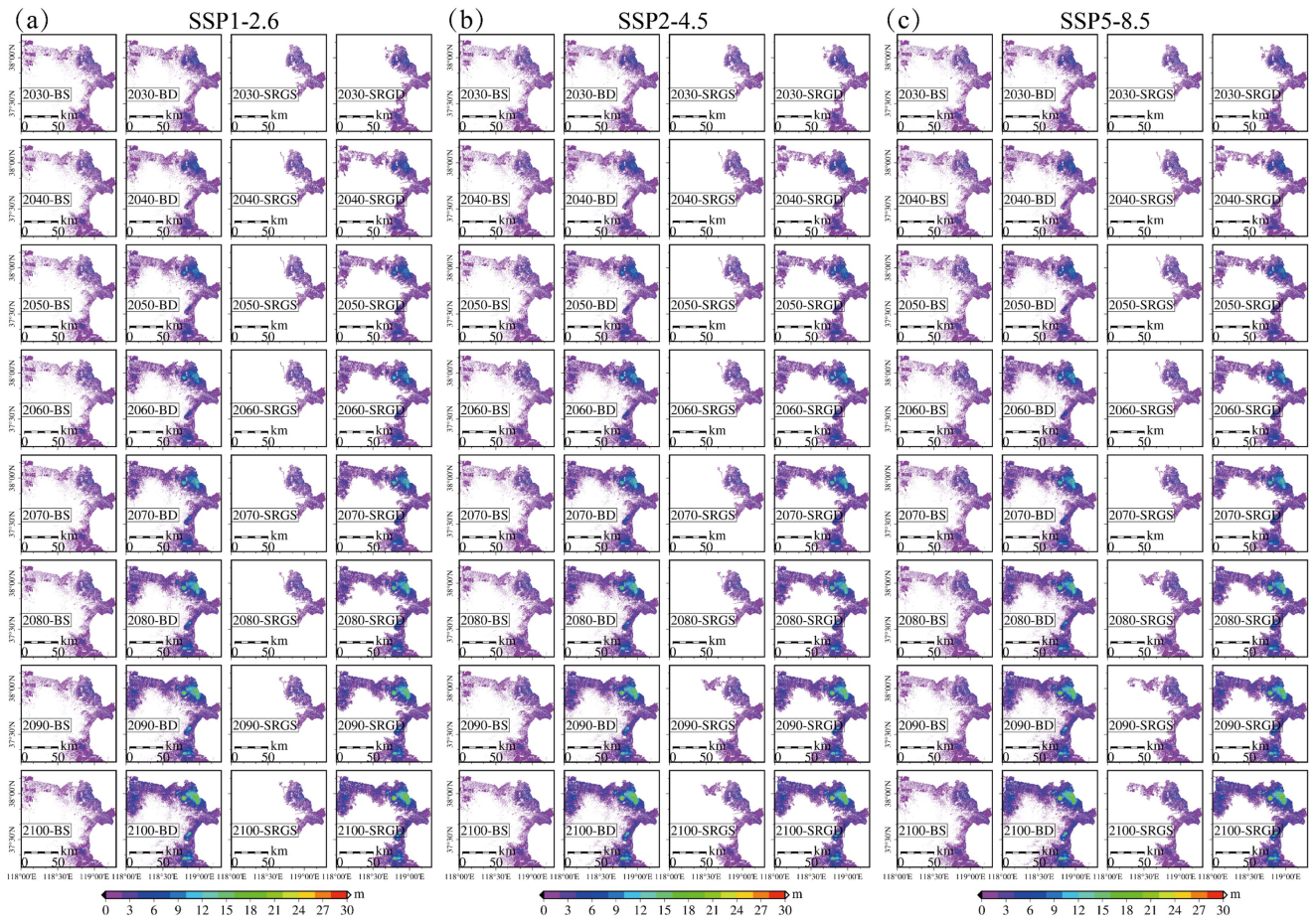
Fig. 10. Two-dimensional raster of the inundated area and depth with time resolution of ten years. Note that the time resolution of the original data is one year. For convenience, the raster data is displayed at an interval of ten years.
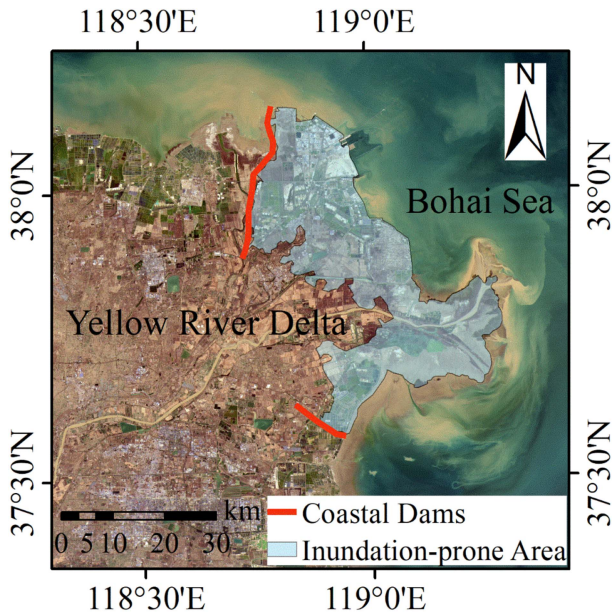

Fig. 11. Inundation-prone areas and future dam sites.

B. Uncertainties of Subsidence and DEM

The surface soil of the YRD is mostly composed of sediments brought by the Yellow river. Thick layers of sediment are consolidated and compacted by chemical and gravitational forces. In addition, the strong influence of local human activities, especially the exploitation of underground brine and oil resources, makes the soft soil easy to sink. Therefore, the coastal subsidence of the YRD is widely distributed, especially serious in some areas due to human activities.

However, there is a weak surface uplift signal in the new land area of the estuary, which is mainly due to the continuous siltation of large amounts of sediment brought by the upper Yellow river [74]. A recent study has also shown that in the Ayeyarwady Delta, Myanmar, unleveed agricultural fields in deltas are less vulnerable to subsidence than leveed or poldered fields [75]. As a result, the rich wetland vegetation in the Yellow River estuary, such as *Suaeda sala*, *Tamarix chinensis*, *Spartina alterniflora*, and *Phragmites australis*, can help capture sediment in a similar way to mangroves or crops, making levee land less likely to sink than levee land.

In addition, relative errors from TS-InSAR observations may also be introduced if the selected reference point is unstable. The

geological conditions along the Yellow River are relatively stable and there are few groundwater and oil exploitation activities. Therefore, the reference point (see Fig. 2) was chosen near the upper reaches of the Yellow River in the study area, namely, the outer edge of the modern YRD, with an elevation higher than 50 m to ensure the minimum relative error.

It is common practice to conduct large-scale flooding studies using open-source DEMs. However, we find that other open source DEMs, such as AW3D30 derived from optical stereo pairs, often have large systematic fringe errors in coastal areas by comparison to InSAR-derived global DEMs (e.g., SRTM). The current DEM can achieve the expected results, while high-resolution TanDEM-X DEM and LiDAR DEM will be more advantageous but more costly [32], [76]. Currently, only the LiDAR technique can guarantee centimeter-level elevation accuracy and spatial resolution, but its cost is unacceptable for large-scale flooding studies. Moreover, the accuracy and reliability of DEM simulation can be further improved with the help of the prediction models and geotechnical models.

V. Conclusion

Coastal subsidence exacerbates relative SLR and increases the risk of coastal flooding and soil salinization. However, the contribution of local subsidence in the YRD to relative SLR is still unclear, and there is a knowledge gap in the inundation scenario of future coastal flooding. In this article, an inundation estimation method combining the ESRG model, InSAR-derived LLS and SLR is applied to the first inundation assessment of the whole YRD with high spatiotemporal resolution. This method can effectively and accurately output coastal delta inundation time series to quantify and characterize changes in inundation area and depth. Compared with the simulation of a single flood, which requires detailed hydrodynamic conditions of the process and evolution, e.g., water velocity, surface roughness and soil moisture content, this article has obvious advantages in studying the changes of global delta inundation area under different SSP scenarios.

The InSAR results show that fast subsiding funnels larger than 50 mm/yr are mainly distributed in the coastal brine mining clusters, and the maximum subsidence rate exceeds 300 mm/yr. Without the construction of coastal dams in recent decades, the low-lying areas are all vulnerable to flooding, with a dramatic increase in the distance of seawater intrusion and the number of inundation events. In addition, recent extraction of brine and oil has clearly increased the likelihood of coastal inundation. If no control measures are taken, the contribution of coastal subsidence to the relative SLR and coastal flooding risk will be at least three times greater than SLR in 2050 under SSP1-2.6, resulting in the increased inundation area and substantial infrastructure damage. Therefore, this article is expected to provide a practical and cost-effective approach for when and how to mitigate land subsidence to prevent future coastal flooding in the YRD.

Acknowledgment

References

[1] P. S. J. Minderhoud, L. Coumou, G. Erkens, H. Middelkoop, and E. Stouthamer, "Mekong delta much lower than previously assumed in sea-level rise impact assessments," *Nature Commun.*, vol. 10, no. 1, Aug. 2019, Art. no. 3847.

[2] J. Syvitski et al., "Sinking deltas due to human activities," *Nature Geosci.*, vol. 2, pp. 681–686, Sep. 2009.

[3] J. P. M. Syvitski, "Deltas at risk," *Sustainability Sci.*, vol. 3, no. 1, pp. 23–32, 2008.

[4] S. A. Kulp and B. H. Strauss, "New elevation data triple estimates of global vulnerability to sea-level rise and coastal flooding," *Nature Commun.*, vol. 10, no. 1, Oct. 2019, Art. no. 4844.

[5] M. Shirzaei and R. Bürgmann, "Global climate change and local land subsidence exacerbate inundation risk to the san Francisco bay area," *Sci. Adv.*, vol. 4, no. 3, 2018, Art. no. eaap9234.

[6] J. D. Restrepo-Ángel et al., "Coastal subsidence increases vulnerability to sea level rise over twenty first century in Cartagena, Caribbean Colombia," *Sci. Rep.*, vol. 11, no. 1, Sep. 2021, Art. no. 18873.

[7] R. J. Nicholls and A. Cazenave, "Sea-level rise and its impact on coastal zones," *Science*, vol. 328, no. 5985, pp. 1517–1520, Jun. 2010.

[8] R. J. Nicholls et al., "A global analysis of subsidence, relative sea-level change and coastal flood exposure," *Nature Climate Change*, vol. 11, no. 4, pp. 338–342, Apr. 2021.

[9] S. J. Williams, "Sea-level rise implications for coastal regions," *J. Coastal Res.*, vol. 63, pp. 184–196, 2013.

[10] D. M. Tralli, R. G. Blom, V. Zlotnicki, A. Donnellan, and D. L. Evans, "Satellite remote sensing of earthquake, volcano, flood, landslide and coastal inundation hazards," *ISPRS J. Photogramm. Remote Sens.*, vol. 59, no. 4, pp. 185–198, Jun. 2005.

[11] E. E. Lentz, E. R. Thieler, N. G. Plant, S. R. Stippa, R. M. Horton, and D. B. Gesch, "Evaluation of dynamic coastal response to sea-level rise modifies inundation likelihood," *Nature Climate Change*, vol. 6, no. 7, pp. 696–700, 2016.

[12] J. Fang et al., "Benefits of subsidence control for coastal flooding in China," *Nature Commun.*, vol. 13, no. 1, Nov. 2022, Art. no. 6946.

[13] H. Xu, X. Hou, D. Li, X. Zheng, and C. Fan, "Projections of coastal flooding under different RCP scenarios over the 21st century: A case study of China's coastal zone," *Estuarine, Coastal Shelf Sci.*, vol. 279, Dec. 2022, Art. no. 108155.

[14] J. Johnston, F. Cassalho, T. Miesse, and C. M. Ferreira, "Projecting the effects of land subsidence and sea level rise on storm surge flooding in coastal North Carolina," *Sci. Rep.*, vol. 11, no. 1, Nov. 2021, Art. no. 21679.

[15] E. Blackwell, M. Shirzaei, C. Ojha, and S. Werth, "Tracking California's sinking coast from space: Implications for relative sea-level rise," *Sci. Adv.*, vol. 6, no. 31, 2020, Art. no. eaba4551.

[16] J. Yin et al., "Long-term flood-hazard modeling for coastal areas using InSAR measurements and a hydrodynamic model: The case study of Lingang New City, Shanghai," *J. Hydrol.*, vol. 571, pp. 593–604, 2019.

[17] P. P. C. Aucelli et al., "Coastal Inundation risk assessment due to subsidence and sea level rise in a Mediterranean alluvial plain (Volturno coastal plain – Southern Italy)," *Estuarine, Coastal Shelf Sci.*, vol. 198, pp. 597–609, Nov. 2017.

[18] M. Shirzaei, J. Freymueller, T. E. Törnqvist, D. L. Galloway, T. Dura, and P. S. J. Minderhoud, "Measuring, modelling and projecting coastal land subsidence," *Nature Rev. Earth Environ.*, vol. 2, no. 1, pp. 40–58, Jan. 2021.

[19] G. Wang et al., "Coastal dam inundation assessment for the Yellow river delta: Measurements, analysis and scenario," *Remote Sens.*, vol. 12, no. 21, pp. 3658–3689, 2020.

[20] E. Gebremichael, M. Sultan, R. Becker, M. El Bastawesy, O. Cherif, and M. Emil, "Assessing Land Deformation and Sea Encroachment in the Nile delta: A radar interferometric and inundation modeling approach," *J. Geophys. Res., Solid Earth*, vol. 123, no. 4, pp. 3208–3224, 2018.

[21] S. Brown, S. Hanson, and R. Nicholls, "Implications of sea-level rise and extreme events around Europe: A review of coastal energy infrastructure," *Climatic Change*, vol. 122, pp. 81–95, Nov. 2014.

[22] G. Herrera-García et al., "Mapping the global threat of land subsidence," *Science*, vol. 371, no. 6524, pp. 34–36, Jan. 2021.

[23] Q. Zhu et al., "Spatiotemporal changes of coastline over the Yellow river delta in the previous 40 years with optical and SAR remote sensing," *Remote Sens.*, vol. 13, no. 10, pp. 1940–1967, 2021.

[24] P. Berardino, G. Fornaro, R. Lanari, and E. Sansosti, "A new algorithm for surface deformation monitoring based on small baseline differential SAR interferograms," *IEEE Trans. Geosci. Remote Sens.*, vol. 40, no. 11, pp. 2375–2383, Nov. 2002, doi: 10.1109/TGRS.2002.803792.

[25] A. Ferretti, A. Fumagalli, F. Novali, C. Prati, F. Rocca, and A. Rucci, "A new algorithm for processing interferometric data-stacks: SqueeSAR," *IEEE Trans. Geosci. Remote Sens.*, vol. 49, no. 9, pp. 3460–3470, Sep. 2011, doi: 10.1109/tgrs.2011.2124465.

[26] A. Ferretti, C. Prati, and F. Rocca, "Nonlinear subsidence rate estimation using permanent scatterers in differential SAR interferometry," *IEEE Trans. Geosci. Remote Sens.*, vol. 38, no. 5, pp. 2202–2212, Sep. 2000, doi: 10.1109/36.868878.

[27] R. Lanari, O. Mora, M. Manunta, J. J. Mallorqui, P. Berardino, and E. Sansosti, "A small-baseline approach for investigating deformations on full-resolution differential SAR interferograms," *IEEE Trans. Geosci. Remote Sens.*, vol. 42, no. 7, pp. 1377–1386, Jul. 2004, doi: 10.1109/tgrs.2004.828196.

[28] G. Wang, P. Li, Z. Li, C. Liang, and H. Wang, "Coastal subsidence detection and characterization caused by brine mining over the Yellow river delta using time series InSAR and PCA," *Int. J. Appl. Earth Observ. Geoinf.*, vol. 114, Nov. 2022, Art. no. 103077.

[29] P. D. Bates, M. S. Horritt, and T. J. Fewtrell, "A simple inertial formulation of the shallow water equations for efficient two-dimensional flood inundation modelling," *J. Hydrol.*, vol. 387, no. 1-2, pp. 33–45, 2010.

[30] C. H. Theiling and J. T. Burant, "Flood inundation mapping for integrated floodplain management: Upper Mississippi river system," *River Res. Appl.*, vol. 29, no. 8, pp. 961–978, 2013.

[31] J. Yin et al., "Flood risks in sinking delta cities: Time for a reevaluation?," *Earth's Future*, vol. 8, no. 8, 2020, Art. no. e2020EF001614.

[32] D. B. Gesch, "Best practices for elevation-based assessments of sea-level rise and coastal flooding exposure," *Front. Earth Sci.-Switzerland*, vol. 6, 2018, Art. no. 2021001.

[33] A. Yunus, R. Avtar, S. Kraines, M. Yamamuro, F. Lindberg, and C. Grimmond, "Uncertainties in tidally adjusted estimates of sea level rise flooding (bathtub model) for the greater London," *Remote Sens.*, vol. 8, no. 5, 2016, Art. no. 366.

[34] J. Fan, G. Zeng, M. Body, and M. - S. Hacid, "Seeded region growing: An extensive and comparative study," *Pattern Recognit. Lett.*, vol. 26, no. 8, pp. 1139–1156, 2005.

[35] U. C. Nkwunonwo, M. Whitworth, and B. Baily, "A review of the current status of flood modelling for urban flood risk management in the developing countries," *Sci. Afr.*, vol. 7, 2020, Art. no. 36201.

[36] J. Teng, A. J. Jakeman, J. Vaze, B. F. W. Croke, D. Dutta, and S. Kim, "Flood inundation modelling: A review of methods, recent advances and uncertainty analysis," *Environ. Model. Softw.*, vol. 90, pp. 201–216, 2017.

[37] D. Gesch et al., "Inundation exposure assessment for Majuro atoll, republic of the Marshall Islands using a high-accuracy digital elevation model," *Remote Sens.*, vol. 12, no. 1, 2020, Art. no. 154.

[38] C. Tu et al., "Synergetic classification of coastal wetlands over the Yellow river delta with gf-3 full-polarization SAR and zhuhai-1 OHS hyperspectral remote sensing," *Remote Sens.*, vol. 13, no. 21, pp. 4444–4467, 2021.

[39] J. Liu et al., "Spatiotemporal change detection of coastal wetlands using multi-band SAR coherence and synergetic classification," *Remote Sens.*, vol. 14, no. 11, 2022, Art. no. 2610.

[40] M. Chang, P. Li, Y. Sun, H. Wang, and Z. Li, "Mapping dynamic turbidity maximum zone of the yellow river estuary from 38 years of Landsat imagery," *Remote Sens.*, vol. 14, no. 15, 2022, Art. no. 3782.

[41] M. Chang, P. Li, Z. Li, and H. Wang, "Mapping tidal flats of the Bohai and Yellow seas using time series Sentinel-2 images and Google earth engine," *Remote Sens.*, vol. 14, no. 8, 2022, Art. no. 1789.

[42] X. Ma et al., "Trait and density responses of Spartina Alterniflora to inundation in the Yellow river delta, China," *Mar. Pollut. Bull.*, vol. 146, pp. 857–864, Sep. 2019.

[43] C. Kuenzer, I. Klein, T. Ullmann, E. F. Georgiou, R. Baumhauer, and S. Dech, "Remote sensing of river delta inundation: Exploiting the potential of coarse spatial resolution, temporally-Dense MODIS time series," *Remote Sens.*, vol. 7, no. 7, pp. 8516–8542, Jul. 2015.

[44] Y. S. Fan et al., "Changes of inundation frequency in the Yellow river delta and its response to wetland vegetation," *Land*, vol. 11, no. 10, Oct. 2022, Art. no. 1647.

[45] *IPCC, Climate Change 2021: The Physical Science Basis. Contribution of Working Group I to the Sixth Assessment Report of the Intergovernmental Panel On Climate Change*. Cambridge, MA, USA: Cambridge Univ. Press, 2021, doi: 10.1017/9781009157896.

[46] M. Lazecký et al., "LiCSAR: An automatic InSAR tool for measuring and monitoring tectonic and volcanic activity," *Remote Sens.*, vol. 12, no. 15, pp. 2430–2459, 2020.

[47] Y. Morishita, M. Lazecky, T. Wright, J. Weiss, J. Elliott, and A. Hooper, "LiCSBAS: An open-source InSAR time series analysis package integrated with the LiCSAR automated sentinel-1 InSAR processor," *Remote Sens.*, vol. 12, no. 3, pp. 424–453, 2020.

[48] P. Li et al., "Impacts of geoid height on large-scale crustal deformation mapping with InSAR observations," *Chin. J. Geophys.-Chin. Ed.*, vol. 56, no. 6, pp. 1857–1867, 2013.

[49] Z. H. Li, E. J. Fielding, and P. Cross, "Integration of insar time-series analysis and water-vapor correction for mapping postseismic motion after the 2003 bam (Iran) earthquake," *IEEE Trans. Geosci. Remote Sens.*, vol. 47, no. 9, pp. 3220–3230, Sep. 2009.

[50] R. Jolivet et al., "Improving InSAR geodesy using global atmospheric models," *J. Geophys. Res., Solid Earth*, vol. 119, no. 3, pp. 2324–2341, 2014.

[51] H. Fattahi and F. Amelung, "InSAR bias and uncertainty due to the systematic and stochastic tropospheric delay," *J. Geophys. Res., Solid Earth*, vol. 120, no. 12, pp. 8758–8773, 2015.

[52] Y. N. Lin et al., "High interseismic coupling in the Eastern Makran (Pakistan) subduction zone," *Earth Planet. Sci. Lett.*, vol. 420, no. 1, pp. 116–126, Jun. 2015.

[53] Z. Yunjun, H. Fattahi, and F. Amelung, "Small baseline InSAR time series analysis: Unwrapping error correction and noise reduction," *Comput. Geosci.*, vol. 133, Dec. 2019, Art. no. 104331.

[54] C. Yu, Z. Li, N. T. Penna, and P. Crippa, "Generic atmospheric correction model for interferometric synthetic aperture radar observations," *J. Geophys. Res., Solid Earth*, vol. 123, no. 10, pp. 9202–9222, 2018.

[55] C. Liang, P. Agram, M. Simons, and E. J. Fielding, "Ionospheric correction of InSAR time series analysis of C-band sentinel-1 TOPS data," *IEEE Trans. Geosci. Remote Sens.*, vol. 57, no. 9, pp. 6755–6773, Sep. 2019, doi: 10.1109/tgrs.2019.2908494.

[56] G. Gomba, F. R. González, and F. D. Zan, "Ionospheric phase screen compensation for the sentinel-1 TOPS and ALOS-2 ScanSAR modes," *IEEE Trans. Geosci. Remote Sens.*, vol. 55, no. 1, pp. 223–235, Jan. 2017, doi: 10.1109/TGRS.2016.2604461.

[57] B. Zhang, R. Wang, Y. Deng, P. Ma, H. Lin, and J. Wang, "Mapping the Yellow river delta land subsidence with multitemporal SAR interferometry by exploiting both persistent and distributed scatterers," *ISPRS J. Photogramm. Remote Sens.*, vol. 148, pp. 157–173, Feb. 2019.

[58] Y. Liu et al., "Land subsidence of the Yellow river delta in China driven by river sediment compaction," *Sci. Total Environ.*, vol. 750, Jan. 2021, Art. no. 142165.

[59] S. Higgins, I. Overeem, A. Tanaka, and J. P. M. Syvitski, "Land subsidence at aquaculture facilities in the Yellow river delta, China," *Geophys. Res. Lett.*, vol. 40, no. 15, pp. 3898–3902, 2013.

[60] J. Höhle and M. Höhle, "Accuracy assessment of digital elevation models by means of robust statistical methods," *ISPRS J. Photogramm. Remote Sens.*, vol. 64, no. 4, pp. 398–406, 2009.

[61] P. Li, Z. Li, K. Dai, Y. Al-Husseinawi, W. Feng, and H. Wang, "Reconstruction and evaluation of DEMs from bistatic tandem-X SAR in mountainous and coastal areas of China," *IEEE J. Sel. Topics Appl. Earth Observ. Remote Sens.*, vol. 14, pp. 5152–5170, 2021, doi: 10.1109/JSTARS.2021.3073782.

[62] H. J. Zwally et al., "ICESat's laser measurements of polar ice, atmosphere, ocean, and land," *J. Geodyn.*, vol. 34, no. 3–4, pp. 405–445, Oct. 2002.

[63] P. Liu, Q. Li, Z. Li, T. Hoey, Y. Liu, and C. Wang, "Land subsidence over oilfields in the Yellow river delta," *Remote Sens.*, vol. 7, no. 2, pp. 1540–1564, 2015.

[64] Y. Liu, H. Huang, and J. Dong, "Large-area land subsidence monitoring and mechanism research using the small baseline subset interferometric synthetic aperture radar technique over the Yellow river delta, China," *J. Appl. Remote Sens.*, vol. 9, no. 1, 2015, Art. no. 096019.

[65] M. Peng, C. Zhao, Q. Zhang, Z. Lu, L. Bai, and W. Bai, "Multi-scale and multi-dimensional time series InSAR characterizing of surface deformation over Shandong Peninsula, China," *Appl. Sci.*, vol. 10, no. 7, pp. 2294–2313, 2020.

[66] H. Abdi and L. J. Williams, "Principal component analysis," *Comput. Statist.*, vol. 2, no. 4, pp. 433–459, 2010.

[67] E. Chaussard, R. Bürgmann, M. Shirzaei, E. J. Fielding, and B. Baker, "Predictability of hydraulic head changes and characterization of aquifer-system and fault properties from InSAR-derived ground deformation," *J. Geophys. Res., Solid Earth*, vol. 119, no. 8, pp. 6572–6590, 2014.

[68] S. Karimzadeh, M. Matsuoka, and F. Ogushi, "Spatiotemporal deformation patterns of the lake Urmia causeway as characterized by multisensor InSAR analysis," *Sci. Rep.*, vol. 8, no. 1, pp. 5357–5367, Apr. 2018.

[69] M. L. Rudolph, M. Shirzaei, M. Manga, and Y. Fukushima, "Evolution and future of the Lusi mud eruption inferred from ground deformation," *Geophys. Res. Lett.*, vol. 40, no. 6, pp. 1089–1092, 2013.

[70] P. P. Ciro Aucelli et al., "Coastal inundation risk assessment due to subsidence and sea level rise in a Mediterranean alluvial plain (Volturno coastal plain Southern Italy)," *Estuarine, Coastal Shelf Sci.*, vol. 198, pp. 597–609, 2017.

[71] R. Adams and L. Bischof, "Seeded region growing," *IEEE Trans. Pattern Anal. Mach. Intell.*, vol. 16, no. 6, pp. 641–647, Jun. 1994, doi: 10.1109/34.295913.

[72] A. Mehnert and P. Jackway, "An improved seeded region growing algorithm," *Pattern Recognit. Lett.*, vol. 18, no. 10, pp. 1065–1071, Oct. 1997.

[73] F. Y. Shih and S. Cheng, "Automatic seeded region growing for color image segmentation," *Image Vis. Comput.*, vol. 23, no. 10, pp. 877–886, 2005.

[74] X. Wu et al., "Stepwise morphological evolution of the active yellow river (Huanghe) delta lobe (1976–2013): Dominant roles of riverine discharge and sediment grain size," *Geomorphology*, vol. 292, pp. 115–127, Sep. 2017.

[75] H. E. Glover et al., "Can unleveed agricultural fields in deltas keep pace with sea-level rise?," *Geophys. Res. Lett.*, vol. 50, no. 3, Feb. 2023, Art. no. e2022GL101733.

[76] S. Kulp and B. H. Strauss, "Global DEM errors underpredict coastal vulnerability to sea level rise and flooding," *Front. Earth Sci. Switzerland*, vol. 4, 2016, Art. no. 205240.

Guoyang Wang received the B.Sc. degree in geodesy from the Shandong Agricultural University, Taian, China, in 2013, and the M.Sc. degree in engineering surveying and remote sensing from the Shandong University of Science and Technology, Qingdao, China, in 2015, and the Ph.D. degree in marine geology from the Ocean University of China, Qingdao, China, in 2023. He is currently a Postdoctoral Fellow with the Ocean University of China.

His research interests include radar interferometry, coastal subsidence, machine learning, coastal flooding, and inundation modeling.
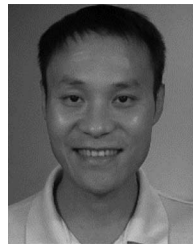
Cunren Liang received the B.S. degree in geodesy from the Shandong University of Science and Technology, Qingdao, China, in 2008, and the Ph.D. degree in photogrammetry and remote sensing from Peking University, Beijing, China, in 2014.

He was a NASA Postdoctoral Program Fellow with the Jet Propulsion Laboratory, Pasadena, CA, USA, from 2015 to 2018, and a Staff Scientist with the California Institute of Technology, Pasadena, CA, USA, from 2018 to 2021. He is currently an Assistant Professor with the School of Earth and Space Sciences, Peking University. His research interests include the technical development of synthetic aperture radar processing, interferometric SAR, and their applications in geoscience and natural hazards response.

Dr. Liang is a Member of the American Geophysical Union. He was a recipient of the NASA Group Achievement Award in 2016, and the JPL Outstanding Postdoctoral Research Award in 2017.

Houjie Wang received the B.Sc. degree in coastal engineering and the Ph.D. degree in marine geology from Ocean University of China, Qingdao, China, in 1996 and 2002, respectively.

He was an Academic Visitor with the University of New South Wales, Sydney, NSW, Australia, in 2008, and the North Carolina State University, Raleigh, NC, USA, in 2006. He is currently a Professor and the Dean with the College of Marine Geoscience, Ocean University of China, Qingdao, China. His research interests include global change, earth observation, coastal and river delta vulnerability.

Dr. Wang has been supported by the National Science Foundation for Distinguished Young Scholars of China, since 2015.

Peng Li received the B.Sc. degree in geodesy from the Changchun Institute of Technology, Changchun, China, in 2007, and the Ph.D. degree in geodesy and geomatics from the Wuhan University, Wuhan, China, in 2013.

He was a visiting Ph.D. student with the University of Glasgow, Glasgow, U.K., in 2012, and a Postdoctoral Fellow with the Ocean University of China, from 2016 to 2019, and an Academic Visitor with the Newcastle University, Newcastle upon Tyne, U.K., in 2019. He is currently an Associate Professor of coastal remote sensing with the Institute of Estuarine and Coastal Zone, Ocean University of China, Qingdao¸ China. He has more than 15 years of research experiences in earth observations, e.g., GNSS, UAV LiDAR, SAR, multispectral, and hyperspectral remote sensing. His research interests include radar interferometry and coastal subsidence, coastal inundation and vulnerability, machine learning and land cover mapping, wetlands change detection with remote sensing time series.

Zhenhong Li (Senior Member, IEEE) received the B.Eng. degree in geodesy from the Wuhan Technical University of Surveying and Mapping (now Wuhan University), Wuhan, China, in 1997, and the Ph.D. degree in GPS, geodesy, and navigation from University College London, London, U.K., in 2005.

He is currently a Professor of imaging geodesy at the College of Geological Engineering and Geomatics, Changan University, Xian, China, and the Director with Big Data Center for Geosciences and Satellites (BDCGS), Xian, and the Director of the Key Laboratory of Western Chinas Mineral Resource and Geological Engineering, Ministry of Education, Xian. He is also a Visiting Professor with the School of Engineering, Newcastle University. He is also the Principal Investigator of the Generic Atmospheric Correction Online Service (GACOS) for interferometric synthetic aperture radar. His research interests include imaging geodesy and its applications to geohazards (e.g., earthquakes, landslides, and land subsidence) and precision agriculture.

Dr. Li is a Fellow of the International Association of Geodesy and an Associate Editor for Advances in Space Research as well as Remote Sensing.